Fractal Web Design of a Hemispherical Photodetector Array with Organic-Dye-Sensitized Graphene Hybrid Composites

Eun Kwang Lee, Ratul Kumar Baruah, Jung Woo Leem, Woohyun Park, Bong Hoon Kim, Augustine Urbas, Zahyun Ku, Young L. Kim, Muhammad Ashraful Alam,* and Chi Hwan Lee*

The vision system of arthropods consists of a dense array of individual photodetecting elements across a curvilinear surface. This compound-eye architecture could be a useful model for optoelectronic sensing devices that require a large field of view and high sensitivity to motion. Strategies that aim to mimic the compound-eye architecture involve integrating photodetector pixels with a curved microlens, but their fabrication on a curvilinear surface is challenged by the use of standard microfabrication processes that are traditionally designed for planar, rigid substrates (e.g., Si wafers). Here, a fractal web design of a hemispherical photodetector array that contains an organic-dye-sensitized graphene hybrid composite is reported to serve as an effective photoactive component with enhanced light-absorbing capabilities. The device is first fabricated on a planar Si wafer at the microscale and then transferred to transparent hemispherical domes with different curvatures in a deterministic manner. The unique structural property of the fractal web design provides protection of the device from damage by effectively tolerating various external loads. Comprehensive experimental and computational studies reveal the essential design features and optoelectronic properties of the device, followed by the evaluation of its utility in the measurement of both the direction and intensity of incident light.

The structural architecture of spider webs found in nature inspires the development of next-generation materials that are capable of efficiently resisting various mechanical loads from environments.[1–3] The fractal web designs that exhibit a repeating pattern on all scale (self-similar) provide unique capabilities to: 1) distribute externally induced stress throughout the threads according to the effective ratio of spiral and radial dimensions; 2) provide greater extensibility to better dissipate force under stretching; and 3) tolerate minor cuts of the threads while maintaining overall strength and function of the entire web architecture.[4–7] Recent studies have demonstrated spider-web-inspired synthetic materials for which the fractal web designs provide an unusual combination of strength and stretchiness while being virtually free of stress concentrations even with few cuts of the spiral threads.[8,9] Although these principles have profound impacts on new design variables for multifunctional or/and multidimensional engineering, the fractal web designs are not well utilized in electronics yet due to the lack of necessary combination of advanced materials, mechanics designs, and system-level integration capabilities for practical application.

Optoelectronic materials and devices deployed across curvilinear surfaces offer qualitatively expanded levels of functionality enabling a large field of view with no aberration, which resembles the compound-eye vision system of arthropods.[10–16] These 3D optoelectronic architectures are particularly attractive for photodetection systems that require a large field of view and wide-angle antireflection.[14,17,18] To engineer a compound-eye-mimicking system,

Dr. E. K. Lee, Dr. J. W. Leem, Prof. Y. L. Kim
Weldon School of Biomedical Engineering
Purdue University
West Lafayette, IN 47907, USA

Prof. R. K. Baruah
Department of Electronics and Communication Engineering
Tezpur University
Tezpur, Assam 784028, India

Prof. R. K. Baruah, Prof. M. A. Alam
Department of Electrical and Computer Engineering
Purdue University
West Lafayette, IN 47907, USA
E-mail: alam@purdue.edu

W. Park
School of Mechanical Engineering
Purdue University
West Lafayette, IN 47907, USA

Prof. B. H. Kim
Department of Organic Materials and Fiber Engineering
Soongsil University
Seoul 06978, South Korea

Dr. A. Urbas, Dr. Z. Ku
Materials and Manufacturing Directorate
Air Force Research Laboratory
Wright-Patterson AFB, Dayton, OH 45433, USA

Prof. C. H. Lee
Weldon School of Biomedical Engineering
School of Mechanical Engineering
School of Materials Engineering
Purdue University
West Lafayette, IN 47907, USA
E-mail: lee2270@purdue.edu

the most promising procedures involve direct printing of photosensitive pixels on curved or hemispherical surfaces in a carefully-aligned manner.[19,20] These efforts pave the way for realizing various 3D forms of photodetectors, but progress in this area is impeded by the complexity of assembling high-performance optoelectronic devices and components onto non-planar surfaces at the microscale and matching the shape of photodetector array with the fixed curvature. Besides, these approaches primarily use Si-based photodetectors, while leaving opportunities to explore zero-bandgap materials, such as graphene, for a faster and wider range of spectral responses.

Graphene, due to its superior carrier mobility and atomically thin nature, provides unmatched optoelectronic properties that offer constant optical absorption coefficient from visible to infrared wavelengths.[21,22] In addition, the excellent mechanical flexibility of graphene warrants its implementation into complex 3D architectures such as controllably-buckled or crumpled thin films, springs, and hinges.[23–26] However, the photosensitivity of graphene is limited by the atomically thin body that allows absorbing light only as low as 2.3% over a wide spectral range.[27] This material limitation impedes its practical application in photodetector systems.

Here, we explore the use of a spider-web-inspired fractal design in the development of a hemispherical photodetector array using an organic-dye-sensitized graphene hybrid composite, with a focused application in high-performance 3D photodetection. Specifically, the hybrid composite material is composed of chemical vapor deposition (CVD)-grown graphene and water-soluble organic cation dyes, which offers enhanced optical light absorption along with desired mechanical flexibility and optoelectronic performances.[28] The fabrication of the photodetector array occurs on a planar Si wafer using traditional microfabrication methods, followed by their deterministic assembly with various sizes of transparent hemispherical domes through a wet transfer printing technique.[29] The overall device layout is shaped into a form that mimics a planar orb web of garden spiders (e.g., Araneus diadematus) for which it effectively adopts the mechanical mismatch during its integration across the hemispherical surface.[30,31] We conducted comprehensive experimental and computational studies to reveal the underlying mechanical and optoelectrical properties of the hemispherical photodetector array, followed by system-level demonstration to evaluate its performance on simultaneous detection of both direction and intensity of incident light.

Figure 1a provides a schematic illustration of the assembly process for a hemispherical photodetector array. The fabrication began with a Si wafer coated with thin films of Ni (100 nm-thick) and polyimide (PI, 3 μm-thick) to serve as a separation and a supporting layer, respectively. The fabrication of the photodetector array was then completed through sequential deposition and patterning of an epoxy-based negative photoresist (e.g., SU-8), Pyronin B (PyB)-doped graphene sheet, dielectric layer (e.g., Al_2O_3), and metal electrodes (e.g., Pd and Au) on top of the PI layer (Figure 1a, left). Here, the mole concentration of PyB was adjusted within a range from 1×10^{-6} M to 1×10^{-3} M in water to form strong π–π interactions with graphene and thereby enhance optical light absorptions (Figure S1, Supporting Information).[31] Next, the surface of the radial threads was selectively capped with a transparent silicone elastomer such

as poly(dimethylsiloxane) (PDMS). The entire structure was then immersed in distilled (DI) water at room temperature and gently peeled from the Si wafer using a thermal release tape (Nitto Denko), which resulted in a clean separation of the Ni interlayer from the Si wafer (Figure 1a, middle). This interfacial debonding in water is attributed to the coupling of elastoplastic deformation of adherent thin films and electrostatic reactions with water molecules at the debonding interface.[32,33] Finally, the thermal release tape was removed by applying heat at 80 °C for 3 min, followed by transferring the resulting device architecture onto a transparent hemispherical dome that was molded with PDMS (Figure 1a, right). Details of the entire fabrication procedures are schematically illustrated in Figure S2 (Supporting Information).

Figure 1b shows a representative photograph of the photodetector array that was placed on a transparent hemispherical dome (PDMS) with a base diameter of 15 mm. The fractal web design allowed its nearly seamless integration across the hemispherical surface while a few wrinkles were formed on the edge in order to adopt the difference in overall size. The mechanical robustness of the device allowed it to be detached and attached from/to various sizes of transparent hemispherical domes with a base diameter ranging from 15 to 31 mm without generating damages (Figure S3, Supporting Information). Figure 1c schematically illustrates the overall structural layout of the fractal web design that contains a total of 48-pixel photodetectors at the cross-junctions of the spiral and radial threads. The detailed drawing of their arrangement is shown in Figure S4 (Supporting Information). The inset presents the cross-sectional side view of a single pixel, displaying the constituent materials with their thicknesses and functions. More detailed geometric information and the equivalent circuit diagram of the single-pixel photodetector are shown in Figure S5 (Supporting Information). Figure 1d,e provides a microscopy image and an enlarged schematic to highlight the single-pixel photodetector and the serpentine traces of Au interconnects, respectively. Both the photodetectors and Au interconnects were positioned along the radial threads wherein the relatively thick PDMS capping layer (≈57 μm-thick; Figure S6, Supporting Information) provides mechanical protection, allowing them to experience little strains of < 4% under stretching (Figure 1f). This configuration also allows externally induced forces to be selectively distributed along the spiral and radial threads with the ratio of ≈7 to 1, while maintaining its overall strength and function even with minor cuts of the spiral threads (Figure S7, Supporting Information).

The experimental and finite element analysis (FEA) results in Figure S8a (Supporting Information) show the nonlinear stress-strain relationships of the radial threads under stretching prior to fracture at the stress of 150 MPa. The radial threads show a nearly viscoelastic behavior such that they resist strains at the beginning of stretching but then have nearly linear stress-strain relationships thereafter. Here, the initial nonlinearity appears mainly because of the viscoelastic property of the PI layer in combination with materials of relatively high Young's modulus (E) such as Al_2O_3 ($E = 300$ GPa), graphene ($E = 1.02$ TPa), and metal thin films ($E > 60$ GPa) that enhance mechanical robustness.[34,35] Figure S8b (Supporting Information) presents the maximum strain tolerance of these materials by comparison

**ADVANCED
SCIENCE NEWS**

www.advancedsciencenews.com

**ADVANCED
MATERIALS**

www.advmat.de
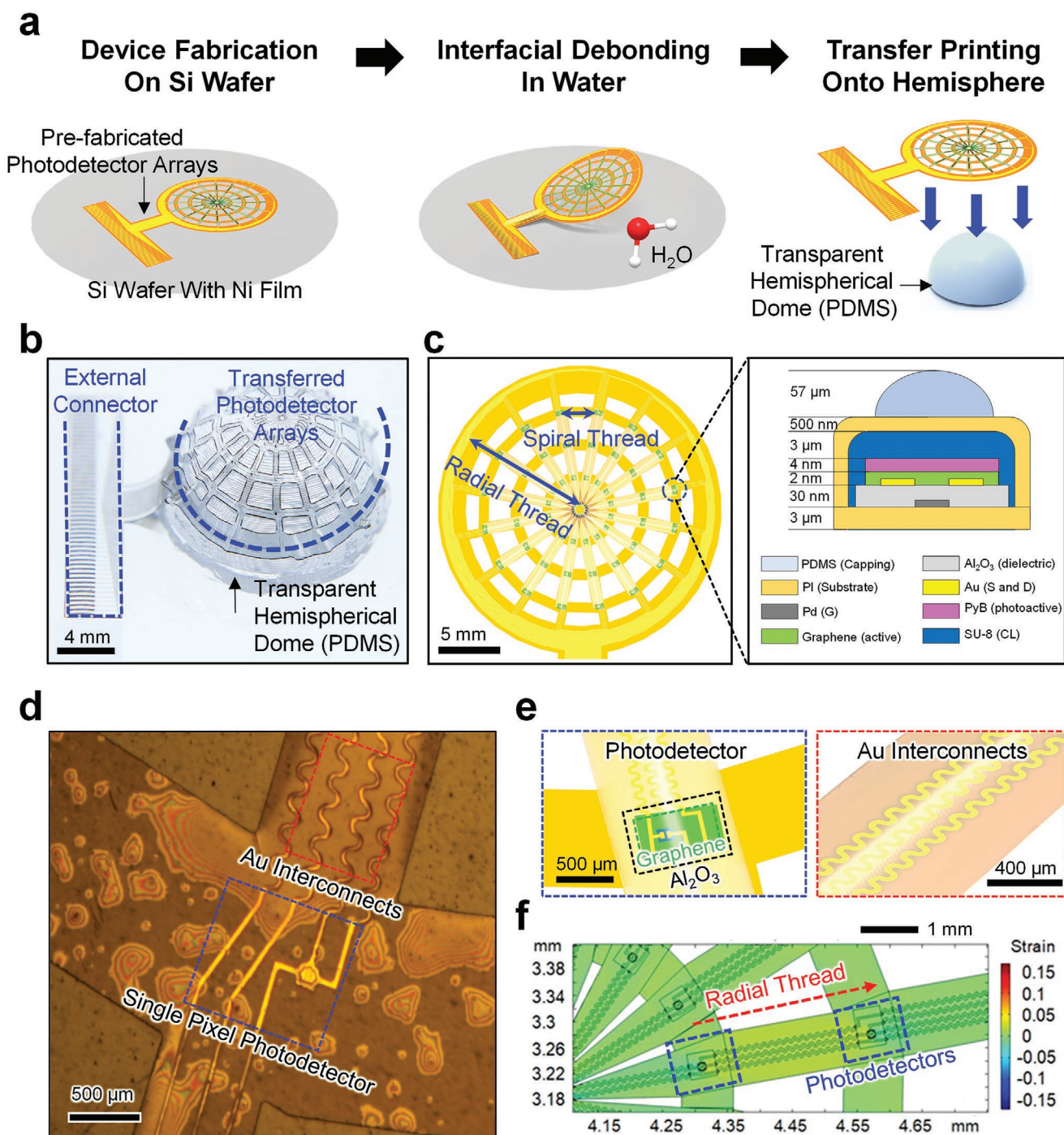
Figure 1. Fabrication method and device layout. a) Schematic illustration of the assembly process for the hemispherical photodetector array. b) Photograph of the device placed on a transparent hemispherical dome (PDMS) with a base diameter of 15 mm. c) Schematic illustration of the structural layout of the fractal web design. The inset shows the cross-sectional side view of the single-pixel photodetector. d) Microscopy image of the single-pixel photodetector. e) Enlarged schematic illustrations of the single-pixel photodetector (left) and the serpentine traces of Au interconnects (right). f) FEA results of the single radial thread under stretching.

with the PI layer when placed on hemispherical PDMS domes with a base diameter ranging from 15 to 31 mm under the stress of 15 MPa. The maximum strain of these materials decreases negligibly with the increased base diameter while the PI layer adopts more strains during their integration because of its substantially lower mechanical modulus than rest of the material layers.

Figure 2a,b presents the transfer and output curves of a single-pixel photodetector placed on a flat surface, respectively. The results show a typical p-type semiconductor behavior due
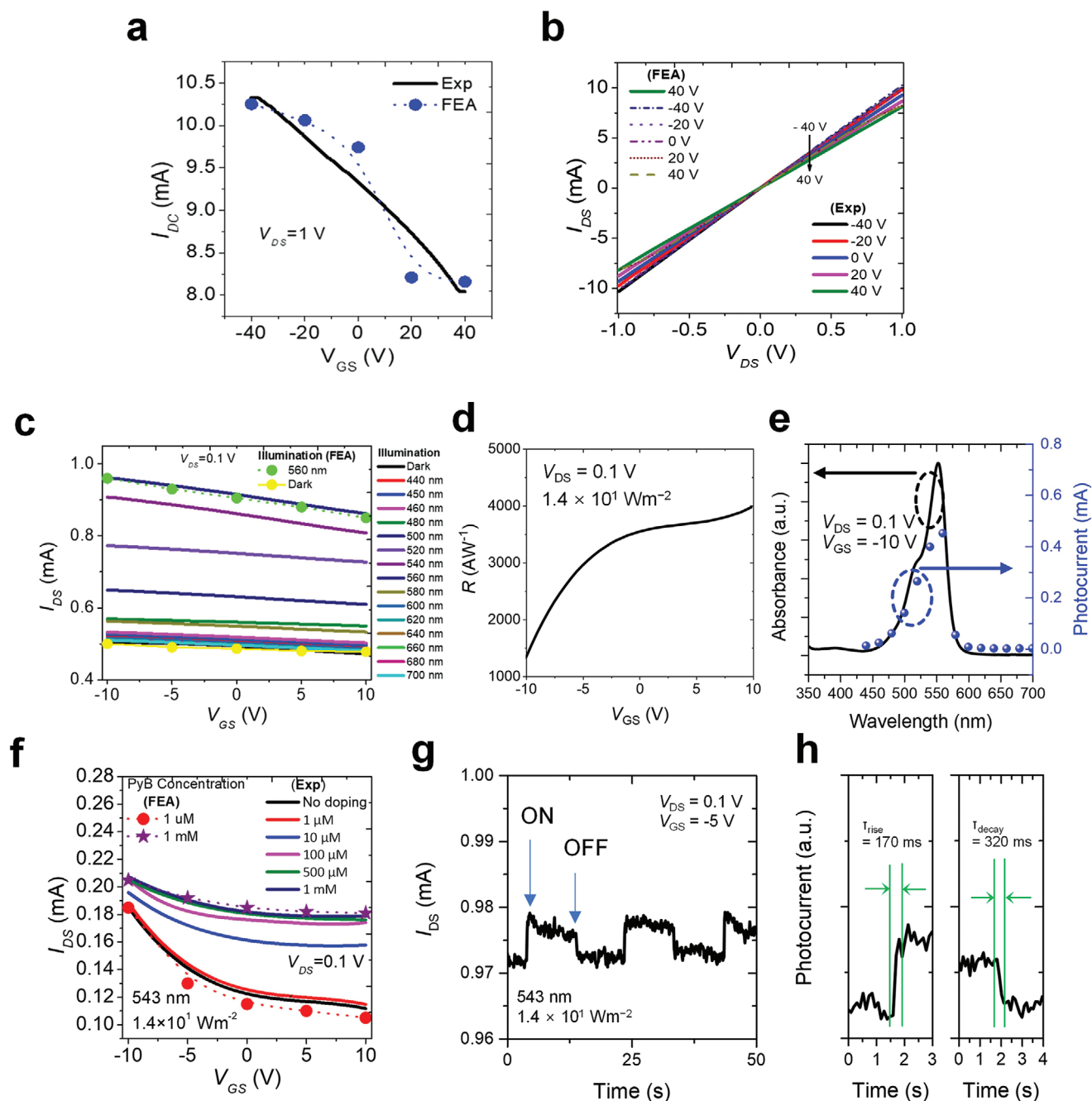
Figure 2. Electrical and optoelectrical characterizations. a,b) Experimental and FEA results of the transfer and output curves of the photodetector when placed on a flat surface, respectively. c) Experimental and FEA results of the corresponding transfer curves as a function of the light wavelength ranging from 440 to 700 nm. d) Plot of R versus V_{GS}. e) Measured absorption spectrum of PyB (black line) and the corresponding photocurrent (blue dots) as a function of the light wavelength ranging from 440 to 700 nm. f) Experimental and FEA results of the corresponding transfer curves as a function of the doping concentration of PyB ranging from 1×10^{-6} M to 1×10^{-3} M. g) Dynamic photoresponsiveness of the photodetector. h) Extracted rising and decay time of the photodetector from (g).

to the presence of oxygen under ambient conditions.[31] The charge carrier mobility (μ) and the subthreshold swing (S) were extracted using the following Equations (1) and (2)

$$\mu = \left[\frac{dI_{DS}}{dV_{GS}}\right]\frac{L}{WC_{ox}V_{DS}} \quad (1)$$

$$S = \frac{dV_{GS}}{d(\log_{10} I_{DS})} \quad (2)$$

where I_{DS} and V_{GS} are source-drain current and source-gate voltage, respectively; dI_{DS}/dV_{GS} is the transconductance (g_m) of the transfer characteristic; L and W are the length and width of the channel, respectively; and C_{ox} is the dielectric capacitance.

The transfer curves shown in Figure S9 (Supporting Information) indicate that the I_{DS} of the photodetector was decreased after the doping of PyB due to the energy transfer caused by strong π–π interactions at the interface.[36] Figure 2c shows the corresponding transfer curves under the ambient conditions with a light wavelength ranging from 440 to 700 nm. The relatively low operation voltage (from −10 to +10 V) is attributed to the high k of the atomic layer deposition (ALD)-deposited Al_2O_3. The drain currents (at $V_{GS} = 0.1$ V) depends on the light wavelength. The ratio (P) of photocurrent (I_{photo}) to dark current (I_{dark}) and the photoresponsivity (R), which are the key parameters of the photodetector, were calculated using the following Equations (3), (4), and (5)

$$I_{photo} = I_{light} - I_{dark} \tag{3}$$

$$P = \frac{I_{photo}}{I_{dark}} \tag{4}$$

$$R = \frac{I_{light} - I_{dark}}{P_{inc} A_{channel}} \tag{5}$$

where I_{light} and I_{dark} are the drain current under illumination and in dark, respectively; P_{inc} is the intensity of incident light; and $A_{channel}$ is the channel area. The plot of R versus V_{GS} is shown in Figure 2d. The photodetector showed substantially high photoresponsivity of >4000 A W^{-1}, which is mainly attributed to the high charge carrier mobility of the graphene ($\approx 1602 \pm 10$ cm^2 V^{-1} s^{-1}).[22] Figure 2e presents the absorption spectrum of the PyB (black line) and the corresponding photocurrent (blue dots) with respect to light wavelength ranging from 440 to 700 nm. The results clearly show that the photoresponse was followed well by the absorption spectrum due to the photocatalytic effect of the PyB which is visible-light-driven photoredox transformations.[37] It is also noted that these organic-dye-sensitized graphene hybrid composites provide high hole current due to the effective gating behavior of the accumulated photoexcited electrons at the interface where the strong π–π interactions occur.[38] As expected, the drain current (I_{DS}) was increased with an increased mole concentration of the PyB from 1×10^{-6} M to 1×10^{-3} M (Figure 2f). Figure 2g,h confirms that the photodetectors are capable of providing repeatable and stable operation upon switching on ($\tau_{rise} = 0.17$ s) and off ($\tau_{decay} = 0.32$ s) under light illumination ($\lambda = 533$ nm; light intensity = 14 W m^{-2}). Throughout these characterizations, the experimental and computational results were in a good match. Importantly, the photocurrent of the device remained nearly unchanged at 653–666 µA with the applied V_{GS} of −5 V under light illumination ($\lambda = 533$ nm; light intensity = 7.9×10^{-2} W m^{-2}) when interfaced with various hemispherical domes with a base diameter ranging from 15 to 31 mm (Figure S10, Supporting Information). These results also confirm that the fractal web design can effectively accommodate mechanical deformations during its integration across the hemispherical surface in a manner that allows the device to experience little strains. Table S1 (Supporting Information) summarizes the key optoelectronic properties of the photodetector compared to those of other similar representatives reported to date.[28,39–42]

Figure 3a shows a measurement setup for the hemispherical photodetector array. This setup contains a parameter analyzer (Keithley 4200A-SCS), optical fibers (Single-Mode Optical Fiber Jumper Code, Duplex), light sources, a stencil shadow mask, and an optical microscope. During the measurement, the device was placed on a flat surface while the direction of incident light was adjusted using the optical fibers at the fixed wavelength and light intensity of 533 nm and 7.9×10^{-2} W m^{-2}, respectively. A stencil shadow mask with a pre-defined pattern, such as a letter of "P" (Figure 3b), was used to define the shape of the illuminated area. Figure 3c–f shows the results of photocurrent mapping for representative cases at the applied V_{GS} of −5 V using different stencil shadow masks with the patterns of "P," cross, triangle, and heart symbol, respectively. The average photocurrent and dark current over the illuminated area were 669.1 ± 4.6 µA and 96.05 ± 3.5 µA, respectively. It is noted that the relatively high dark current typically occurs due to the zero-bandgap nature of graphene.[43] These results were consistent with those obtained from a control photodetector array that was fabricated directly on a Si wafer using conventional microfabrication processes (Figure S11, Supporting Information). The spatial resolution of the photodetector array can be further improved by increasing the number of spiral or/and radial threads while maintain the overall size of the device. Figure S12 (Supporting Information) schematically illustrates the relationship between the number of threads and the spatial resolution (in turn, the total number of photodetector pixels).

The hemispherical photodetector array is optically semi-transparent ($\approx$93% at 533 nm) due to the thin thickness (1.5 µm-thick) and wide-open meshes of the fractal web design where light can pass through. Consequently, the device produces two sensing locations at the entry and exit sites with an incident light, enabling simultaneous detection of its direction and intensity. **Figure 4**a schematically illustrates the arrangement of a laser beam source for the device placed on a transparent hemispherical dome (base diameter = 23 mm). Both the azimuthal angle in the x–y plane and the polar angle between the x–y plane and z-direction were fixed at 45° with the distance to the laser beam source (533 nm; 1.4×10^1 W m^{-2}) of 35 cm. Figure 4b shows a representative photograph (left column) and photocurrent mapping results (right column) when the whole area of the device was illuminated. A total of 48-pixel photodetectors responded without failure where the average photocurrent and dark current over the illuminated area were 591.1 ± 5.5 µA and 120.4 ± 9.4 µA, respectively. The photoresponsiveness was stronger on the illuminated side than on the other side due simply to partial reflection and absorption of light by the device. Figure 4c,d shows the corresponding results by focusing the laser beam onto a specific area of the device with the spot size of approximately 10 and 3 mm in diameter, respectively. The results show that the degree of accuracy in determining the position of the laser beam was increased with a decreased spot size. The maximum photocurrents for both cases were about 600 µA, which were increased higher than 1200 µA at the center of the illuminated area when the light intensity was increased to 5.0×10^1 W m^{-2} (Figure S13, Supporting Information).

This work demonstrates the system-level integration of a fractal web design with a hemispherical photodetector
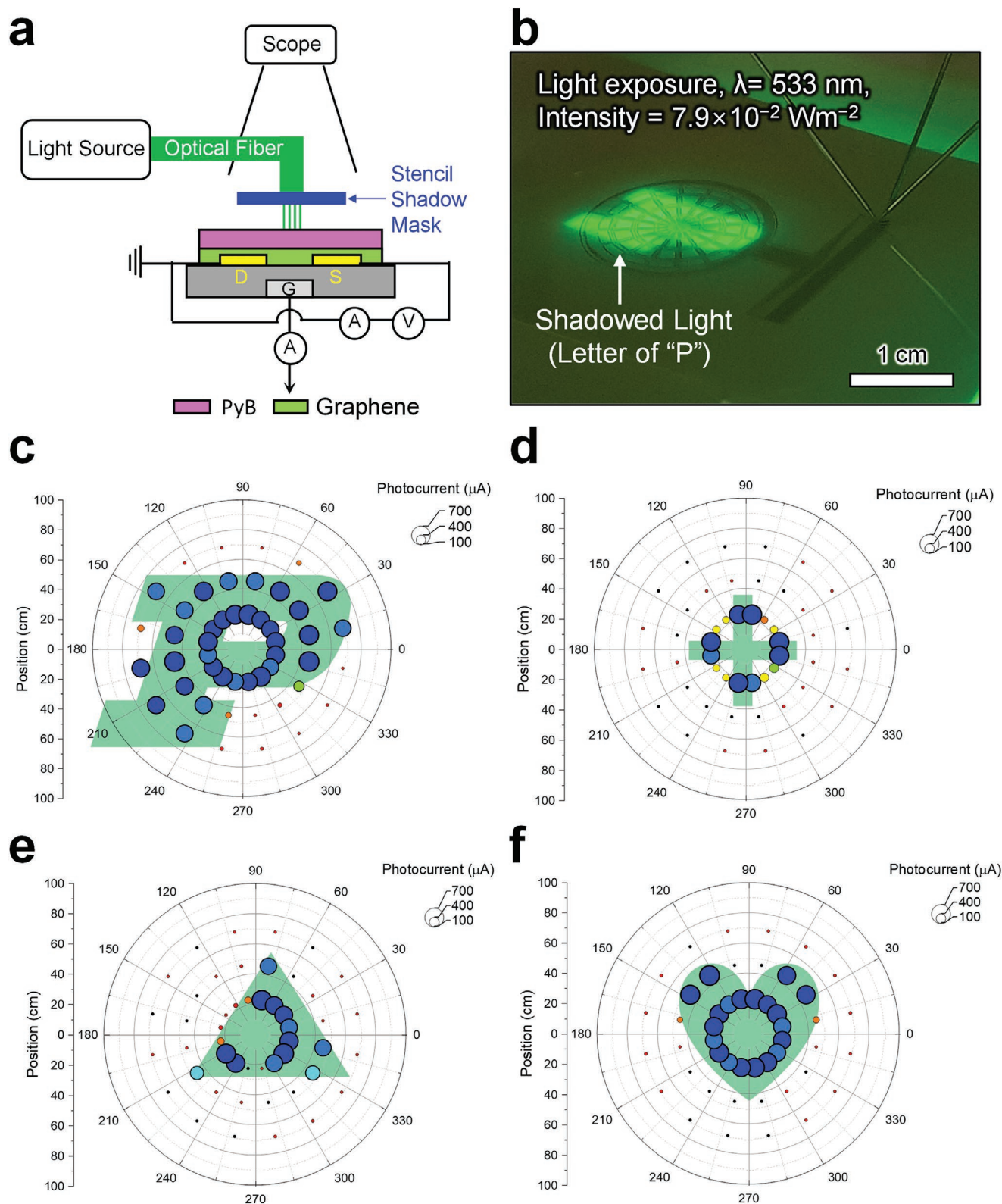
Figure 3. 2D photocurrent mapping. a) Schematic illustration of the measurement setup. b) Photograph of the measurement specimen with a stencil shadow mask with a pre-defined pattern such as a letter "P." c–f) Results of the 2D photocurrent mapping using stencil shadow masks of different patterns such as "P," cross, triangle, and heart symbol, respectively.

ADVANCED
SCIENCE NEWS

www.advancedsciencenews.com

ADVANCED
MATERIALS

www.advmat.de
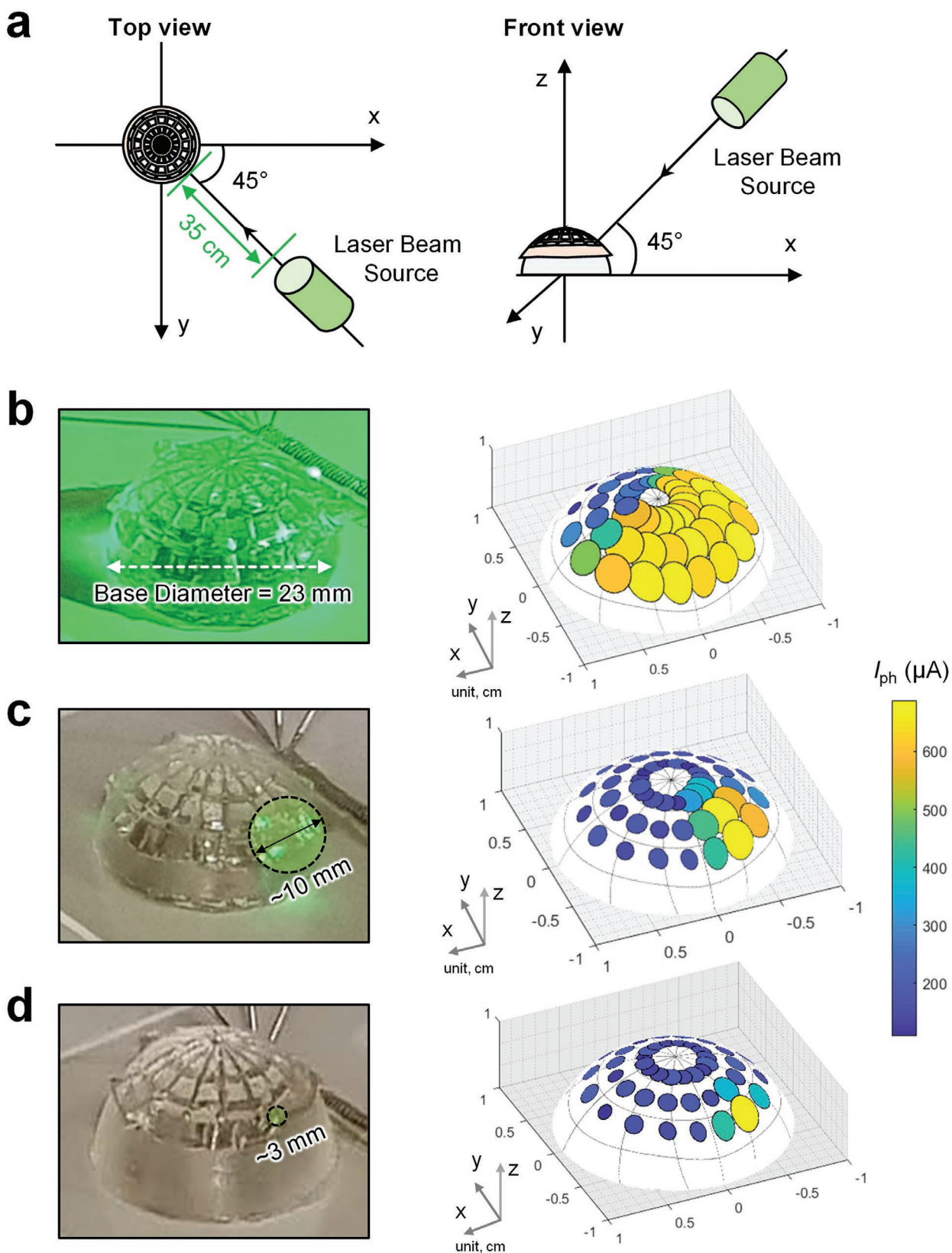
Figure 4. 3D photocurrent mapping. a) Schematic illustration of the measurement setup. b) Representative photograph (left column) and photocurrent mapping results (right column) when the whole area of the device was illuminated. c,d) The corresponding results by focusing the laser beam onto a specific spot of the device with the spot size of approximately 10 and 3 mm in diameter, respectively.

**ADVANCED
SCIENCE NEWS**
www.advancedsciencenews.com

**ADVANCED
MATERIALS**
www.advmat.de

array that incorporates an organic-dye-sensitized graphene, thereby offering several important features, including 1) the desired structural robustness with high threshold strains to avoid damage during its integration across various hemispherical surfaces; 2) the advanced optoelectronic functionality in detecting both direction and intensity of incident light; and 3) the mechanical resilience to arguably large stress (up to 150 MPa) that allows the device to be attached and detached to/from planar or non-planar surfaces in a repetitive manner. In addition, the use of the PyB-doped graphene shows a viable possibility, as a substitute of Si, for a flexible and effective photoactive component with enhanced photoresponsivity (>1000 A W^{-1}). The deterministic assembly process presented herein enables deploying 2D deformable functional materials in 3D device architectures, which may foreshadow new opportunities to better advance the field of 3D electronic and optoelectronic devices.

Experimental Section

A detailed description of procedures and characterization methods are available in the Supporting Information.

Supporting Information

Supporting Information is available from the Wiley Online Library or from the author.

Conflict of Interest

The authors declare no conflict of interest.

Keywords

compound-eye imaging systems, fractal web design, hemispherical photodetector arrays, organic dye-sensitized graphene, wet-transfer printing

[1] F. Bosia, M. J. Buehler, N. M. Pugno, *Phys. Rev. E* **2010**, *82*, 059902.
[2] I. Su, Z. Qin, T. Saraceno, A. Krell, R. Muhlethaler, A. Bisshop, M. J. Buehler, *J. R. Soc., Interface* **2018**, *15*, 20180193.
[3] H. Namazi, *ARC J. Neurosci.* **2017**, *2*, 38.
[4] Q. He, J. Feng, Y. J. Chen, H. G. Zhou, *J. Sandwich Struct. Mater.* **2020**, *22*, 771.
[5] Y. Guo, Z. Chang, B. Li, Z. L. Zhao, H. P. Zhao, X. Q. Feng, H. J. Gao, *Appl. Phys. Lett.* **2018**, *113*, 103701.
[6] Y. Aoyanagi, K. Okumura, *Phys. Rev. Lett.* **2010**, *104*, 038102.
[7] M. Alam, C. Jenkins, *Int. J. Damage Mech.* **2005**, *14*, 365.
[8] X. Liu, D. Liu, J. H. Lee, Q. B. Zheng, X. H. Du, X. Y. Zhang, H. R. Xu, Z. Y. Wang, Y. Wu, X. Shen, J. Cui, Y. W. Ma, J. K. Kim, *ACS Appl. Mater. Interfaces* **2019**, *11*, 2282.
[9] S. W. Cranford, A. Tarakanova, N. M. Pugno, M. J. Buehler, *Nature* **2012**, *482*, 72.
[10] L. L. Gu, S. Poddar, Y. J. Lin, Z. H. Long, D. Q. Zhang, Q. P. Zhang, L. Shu, X. Qiu, M. Kam, A. Javey, Z. Y. Fan, *Nature* **2020**, *581*, 278.
[11] L. C. Kogos, Y. Z. Li, J. N. Liu, Y. Y. Li, L. Tian, R. Paiella, *Nat. Commun.* **2020**, *11*, 1637.
[12] S. H. Park, R. T. Su, J. Jeong, S. Z. Guo, K. Y. Qiu, D. Joung, F. B. Meng, M. C. McAlpine, *Adv. Mater.* **2018**, *30*, 1803980.
[13] M. Juusola, A. Dau, Z. Y. Song, N. Solanki, D. Rien, D. Jaciuch, S. Dongre, F. Blanchard, G. G. de Polavieja, R. C. Hardie, T. Jouni, *Elife* **2017**, *6*, 26117.
[14] I. W. Jung, J. L. Xiao, V. Malyarchuk, C. F. Lu, M. Li, Z. J. Liu, J. Yoon, Y. G. Huang, J. A. Rogers, *Proc. Natl. Acad. Sci. USA* **2011**, *108*, 1788.
[15] K. H. Jeong, J. Kim, L. P. Lee, *Science* **2006**, *312*, 557.
[16] K. Sim, S. Chen, Z. W. Li, Z. Y. Rao, J. S. Liu, Y. T. Lu, S. Jang, F. Ershad, J. Chen, J. L. Xiao, C. J. Yu, *Nat. Electron.* **2019**, *2*, 471.
[17] K. Zhang, Y. H. Jung, S. Mikael, J. H. Seo, M. Kim, H. Y. Mi, H. Zhou, Z. Y. Xia, W. D. Zhou, S. Q. Gong, Z. Q. Ma, *Nat. Commun.* **2017**, *8*, 1782.
[18] Y. M. Song, Y. Z. Xie, V. Malyarchuk, J. L. Xiao, I. Jung, K. J. Choi, Z. J. Liu, H. Park, C. F. Lu, R. H. Kim, R. Li, K. B. Crozier, Y. G. Huang, J. A. Rogers, *Nature* **2013**, *497*, 95.
[19] S. D. Wu, T. Jiang, G. X. Zhang, B. Schoenemann, F. Neri, M. Zhu, C. G. Bu, J. D. Han, K. D. Kuhnert, *Artif. Intell. Rev.* **2017**, *48*, 573.
[20] D. Floreano, R. Pericet-Camara, S. Viollet, F. Ruffier, A. Bruckner, R. Leitel, W. Buss, M. Menouni, F. Expert, R. Juston, M. K. Dobrzynski, G. L'Eplattenier, F. Recktenwald, H. A. Mallot, N. Franceschini, *Proc. Natl. Acad. Sci. USA* **2013**, *110*, 9267.
[21] C. H. Gong, K. Hu, X. P. Wang, P. H. Wangyang, C. Y. Yan, J. W. Chu, M. Liao, L. P. Dai, T. Y. Zhai, C. Wang, L. Li, J. Xiong, *Adv. Funct. Mater.* **2018**, *28*, 1706559.
[22] A. N. Grigorenko, M. Polini, K. S. Novoselov, *Nat. Photonics* **2012**, *6*, 749.
[23] W. Lee, Y. Liu, Y. Lee, B. K. Sharma, S. M. Shinde, S. D. Kim, K. Nan, Z. Yan, M. D. Han, Y. G. Huang, Y. H. Zhang, J. H. Ahn, J. A. Rogers, *Nat. Commun.* **2018**, *9*, 1417.
[24] P. Kang, M. C. Wang, P. M. Knapp, S. Nam, *Adv. Mater.* **2016**, *28*, 4639.
[25] Y. H. Zhang, F. Zhang, Z. Yan, Q. Ma, X. L. Li, Y. G. Huang, J. A. Rogers, *Nat. Rev. Mater.* **2017**, *2*, 17019.
[26] H. H. Cheng, Y. Liang, F. Zhao, Y. Hu, Z. L. Dong, L. Jiang, L. T. Qu, *Nanoscale* **2014**, *6*, 11052.
[27] R. R. Nair, P. Blake, A. N. Grigorenko, K. S. Novoselov, T. J. Booth, T. Stauber, N. M. R. Peres, A. K. Geim, *Science* **2008**, *320*, 1308.
[28] Y. Lee, S. H. Yu, J. Jeon, H. Kim, J. Y. Lee, J. H. Ahn, E. Hwang, J. H. Cho, *Carbon* **2015**, *88*, 165.
[29] D. S. Wie, Y. Zhang, M. K. Kim, B. Kim, S. Park, Y. J. Kim, P. P. Irazoqui, X. L. Zheng, B. X. Xu, C. H. Lee, *Proc. Natl. Acad. Sci. USA* **2018**, *115*, 7236.
[30] C. H. L. Lee, D. R. Kim, X. Zheng, 8815707, **2014**.
[31] E. K. Lee, Y. Kim, J. Back, E. Lee, J. H. Oh, *J. Mater. Chem. C* **2018**, *6*, 6672.
[32] Y. Zhang, B. O. O. Kim, Y. Gao, D. S. Wie, C. H. Lee, B. X. Xu, *Int. J. Solids Struct.* **2019**, *180–181*, 30.

[33] C. Lee, J. Kim, C. Zou, I. Cho, J. Weisse, W. Nemeth, Q. Wang, A. Van Duin, T. Kim, X. Zheng, *Sci. Rep.* **2013**, *3*, 2917.

[34] P. Zhang, L. L. Ma, F. F. Fan, Z. Zeng, C. Peng, P. E. Loya, Z. Liu, Y. J. Gong, J. N. Zhang, X. X. Zhang, P. M. Ajayan, T. Zhu, J. Lou, *Nat. Commun.* **2014**, *5*, 3782.

[35] G. Krautheim, T. Hecht, S. Jakschik, U. Schroder, W. Zahn, *Appl. Surf. Sci.* **2005**, *252*, 200.

[36] J. X. Weng, S. C. Zhao, Z. T. Li, K. B. Ricardo, F. Zhou, H. Kim, H. T. Liu, *Nanomaterials* **2017**, *7*, 337.

[37] S. P. Pitre, C. D. McTiernan, J. C. Scaiano, *ACS Omega* **2016**, *1*, 66.

[38] N. Zhang, L. M. Tong, J. Zhang, *Chem. Mater.* **2016**, *28*, 6426.

[39] C. W. Chiang, G. Haider, W. C. Tan, Y. R. Liou, Y. C. Lai, R. Ravindranath, H. T. Chang, Y. F. Chen, *ACS Appl. Mater. Interfaces* **2016**, *8*, 466.

[40] P. Sahatiya, S. Badhulika, *Nanotechnology* **2017**, *28*, 455204.

[41] M. Kim, P. Kang, J. Leem, S. Nam, *Nanoscale* **2017**, *9*, 4058.

[42] J. Ding, H. J. Fang, Z. P. Lian, Q. R. Lv, J. L. Sun, Q. F. Yan, *Nanoscale* **2018**, *10*, 10538.

[43] S. Fukushima, M. Shimatani, S. Okuda, S. Ogawa, Y. Kanai, T. Ono, K. Inoue, K. Matsumoto, *Opt. Lett.* **2019**, *44*, 2598.